Improving Understanding of Atmospheric River Water Vapor Transport using a Three-Dimensional Straightened Composite Analysis

Guangzhi XU[1], Lin WANG[2], Ping CHANG[3,4], Xiaohui MA[5], Shuyu WANG[5]

[1]College of Global Change and Earth System Science, Beijing Normal University, Beijing, China. ORCID: 0000-0001-5877-5608
[2]Center for Monsoon System Research, Institute of Atmospheric Physics, Chinese Academy of Sciences, Beijing, China
[3]Department of Oceanography and Department of Atmospheric Sciences, Texas A&M University, College Station, Texas, USA
[4]The International Laboratory for High-Resolution Earth System Prediction, Texas A&M University, College Station, Texas, USA
[5]Key Laboratory of Physical Oceanography and Frontiers Science Center for Deep Ocean Multispheres and Earth System, Ocean University of China / Qingdao Pilot National Laboratory for Marine Science and Technology, Qingdao, China

Key Points:

- Develops a new method to composite atmospheric rivers with irregular shapes and orientations.
- Reveals the meso-scale secondary circulation across the atmospheric river and highlights the relationship with frontogenesis processes.
- Depicts the 3D structure of moisture transports within an atmospheric river and the different geostrophic and ageostrophic contributions.

Corresponding author: Guangzhi XU, xugzhi1987@gmail.com

Abstract

The irregular shapes of atmospheric rivers (ARs) and the scarcity of sounding data have hampered easy AR composite analyses and understandings about AR's moisture transport mechanism. In this work we develop a method to composite AR-related variables from a reanalysis dataset. By averaging a large number of samples, the three dimensional structure and some evolutionary features of a typical North Pacific AR are revealed. An AR is typically located along and in front of the surface cold front of an extratropical cyclone. A meso-scale secondary circulation is observed in the cross-sections of the AR corridor, where both geostrophic and ageostrophic winds make indispensable contributions to the strong moisture transport. Geostrophic moisture advection across the cold front within the Equatorward half of the AR is created by the baroclinicity of the system, and serves as the primary moisture source of the AR-resided atmosphere. Moisture fluxes from the warm sector of the cyclone are primarily due to ageostrophic winds within the boundary layer, and are more important within the poleward half the AR, particularly during the genesis stage. The faster movement speed of the AR compared with low level winds enables the ARs to collect downwind moisture. While within the Equatorward half moisture transport is mostly attributed to geostrophic advection carried along by the propagating AR-cyclone couple. Driven by the intensifying geostrophic winds, ARs tend to reach peak moisture transport intensity about two days after genesis. Then reduced moisture and influxes from lateral boundaries prevent further moisture flux intensification.

1 Introduction

Researches on the salient lower tropospheric moisture fluxes, now commonly known as "atmospheric rivers" (ARs), can be dated back to the 1970s (K. A. Browning & Pardoe, 1973). It has also been related to concepts including the warm conveyor belt (WCB), tropical moisture exports and low level jets (LLJs) (e.g. Bao et al. (2006); Knippertz et al. (2013); Zhu and Newell (1998); Gimeno et al. (2014)). As the research matures and ambiguities are being clarified, the community has arrived at the term "atmospheric rivers", with a formal definition of "a long, narrow and transient corridor of strong horizontal water vapor transport that is typically associated with a LLJ stream ahead of the cold front of an extratropical cyclone." (Ralph et al., 2018). This definition summarizes the most prominent features of ARs, and also ties the phenomenon to its key physical driving factors.

A number of earlier works lay the foundations for the understandings of the AR-related physical processes. Newell and Zhu (1994); Zhu and Newell (1994, 1998) suggested a close relationship between ARs and cold fronts, by observing the spatial coincidence of such filamentary structures and extratropical storm tracks. The baroclinicity and humidity gradients associated with frontal systems give rise to a net poleward heat and moisture transport (Zhu & Newell, 1998). A key contributor to the enhanced moisture transport is the pre-frontal LLJ found in the warm sector of an extratropical cyclone (Ralph et al. (2004) and references wherein). To help fully capture the narrow transverse structures of ARs, direct measurements were collected from dropsondes and rawinsondes (Ralph et al., 2004, 2005, 2017). These sounding measurements observationally quantify the amount of water vapor transported by ARs, and also help establish the relationship between ARs and meso-scale frontal structures. A detailed analyses on the development of ARs and frontogenesis processes are given in a case study by Cordeira et al. (2013), using the frontogenesis function to indicate the location and strength of the secondary ageostrophic circulation across the AR corridor. The strengthening effect of frontogenesis on ARs has also been documented by Neiman et al. (2013). On the other hand, Z. Zhang et al. (2019) performed a statistical analysis on the co-occurrences of ARs and extratropical cyclones. Their results showed that 82% of Eastern Pacific ARs are associated with an extratrop-

ical cyclone, and there exists mutual intensification mechanisms between these two phenomena.

However, existing studies on the structures and dynamics of ARs have left some knowledge gaps. Firstly, it is noticed that analyses on the structures or evolutions of ARs have been largely relying on case studies (e.g. Neiman et al. (2013); Bao et al. (2006); Ralph et al. (2005, 2017); Cordeira et al. (2013)). Few studies have analyzed the general dynamical changes following the AR life cycle by taking a large population of ARs into consideration. Based on the averages of Pacific and Atlantic ARs during 2005-2016, Xu et al. (2020a) documented an early intensification and a subsequent weakening of AR IVT during the life cycle, but no physical explanation was given to the possible causes of such a change. Zhou et al. (2018) documented some kinematic characteristics of North Pacific ARs following their life cycle, including their traveled distances, propagation speeds and pathways, yet structural or dynamical analyses are lacking. Secondly, most previous works have focused on the along-AR moisture fluxes/winds in their cross-sectional analyses (e.g. Newell and Zhu (1994); Ralph et al. (2004); Cordeira et al. (2013); Ralph et al. (2017)), and few has analyzed the roles played by the cross-AR fluxes/winds. It has been argued that ARs collect considerable amount of moisture from the surrounding atmosphere (Bao et al., 2006; Cordeira et al., 2013; Dacre et al., 2019), however, it is not clear how the moisture from the lateral boundaries of the AR get aggregated and contributes to the strong AR IVT. The distribution of cross-sectional winds associated with the frontal structure is likely the key to answering this question.

The scarcity of large sample AR composite analyses in literature is largely due to their complex shapes. Unlike tropical cyclones, storms or ocean eddies whose circular symmetry allows for relatively straightforward composite analysis (e.g. Knaff et al. (2014); Jourdain et al. (2014); X. Zhang et al. (2019); Frenger et al. (2013)), the irregular shapes of ARs deny such a convenience. As a work-around, and so motivated by the physical relationship with extratropical cyclones, some studies adopted a cyclone-centric perspective, and created composites by aligning up the extratropical cyclones that are found to have an accompanying AR (Zhu & Newell, 1994; Dacre et al., 2015; Eiras-Barca et al., 2018; Dacre et al., 2019; Z. Zhang et al., 2019). This gives the broad configuration of the AR-cyclone couple. However, the AR and its accompanying cyclone do not form a rigid relationship, but with considerably varying distances (Z. Zhang et al., 2019). Therefore, some of the more delicate meso-scale structures in the cross-sections of the ARs may be lost. On the other hand, sounding observations can provide an accurate cross-sectional view of an AR, but suffer from limitations of data availability and representativeness. Existing literature based on sounding data are spatially confined to the near coastal regions of the Northeastern Pacific, and can not support a full life cycle analysis on long-lived ARs originated from the western Pacific. This may imply a big limitation of this approach, considering that many of the North America landfalling ARs are originated from the Kuroshio Extension region (Liu et al., 2021). The relative roles played by large-scale geostrophic processes and the ageostrophic, secondary frontal circulation can not by revealed using sounding data alone (Ralph et al., 2004). Furthermore, satellite images lack the ability to resolve the vertical structure of the AR, and surface wind speed measurements are often contaminated by heavy precipitation (Ralph et al., 2004).

In view of such limitations, we develop a method to process and "straighten" the AR-related variables in a reanalysis dataset to a composite-ready form. The resultant composites can be used to depict the general three dimensional structure of an AR. We aim to use such information to explain how North Pacific ARs collect moisture from the surrounding atmosphere, their relationship with extratropical cyclones and cold fronts, and how the AR associated IVT is affected by dynamical and thermodynamical changes following their life cycle.

The important role played by ARs in poleward moisture transport has been widely acknowledged (e.g. Zhu and Newell (1998); Ralph et al. (2004); Xu et al. (2020a); Ralph

et al. (2020)). However, the exact manner in which they achieve the transport has raised some debates in literature. There are broadly two competing views regarding the moisture transports by ARs, one suggests a direct transport of moisture from the low latitudes along the corridor of the AR all the way to the mid-latitude target regions (e.g. Newell and Zhu (1994); Wick et al. (2013); Neiman et al. (2013)), and the other emphasizes the local recycling of moisture and the replenishment from tropical and extratropical sources (e.g. Bao et al. (2006); Dacre et al. (2015, 2019)). In particular, Dacre et al. (2019) proposed a "feeder-airstream" mechanism to explain the moisture sources for an AR-cyclone system. However, their composites only cover a 1500 km radius around the cyclone center, and may not provide a complete picture of the AR. Therefore, we also aim to give an AR-centric depiction of the moisture transport pattern, and to offer an answer to the question of how ARs transport moisture in the Earth- and AR-relative frames of reference.

This work is organized follows. Section 2 introduces the dataset and the compositing methods. Section 3 gives analyses on the straightened AR composites, by first showing the typical AR-cyclone relationship in a plane-view perspective in Section 3.1, followed by the cross-sectional views in Section 3.2. The geostrophic and ageostrophic winds have different levels of importance in the along-front and cross-front directions. Their contributions to the thermodynamic and dynamic processes of AR evolutions are discussed in Section 3.3-3.4. The moisture transport pattern by a typical AR is explored in Section 3.5, in the Earth- and AR-relative frames of reference, respectively. The key findings are summarized in Section 4, with some discussions on the implications and limitations of the work.

2 Methodology and data

2.1 Reanalysis data

Three dimensional air temperature (T), geopotential height (Z), specific humidity (q) and winds (u, v and w) during 2004-Jan to 2010-Dec are obtained from ECMWF's ERA-INTERIM (ERA-I) reanalyses product (Dee et al., 2011). All data have a horizontal resolution of 0.75° and a temporal resolution of 6 hours. IVT is computed from layered u, v and q by vertically integrating across the atmosphere column. The choice of the reanalysis product has been shown to be an insignificant factor to AR detection results (Ralph et al., 2018). The 0.75° resolution of ERA-I data is close to the average 80 km dropsonde spacing of Ralph et al. (2017) and is sufficient to resolve cross-sectional structures of ARs.

2.2 AR detection and tracking

ARs at individual time points are detected using the magnitude-independent detection algorithm documented in Xu et al. (2020b). By relaxing the requirement on the IVT magnitude and instead performing the filtering based on the spatio-temporal scales of the ARs, this detection method is less sensitive to parameter choices, and can more reliably retain ARs at the genesis or dissipating stages when their IVT strengths are generally weaker. The same AR entity appearing in consecutive time slices are tracked using the "simple-path" tracking method as introduced in Xu et al. (2020b).

2.3 AR straightening method for scalar fields

To create composites of ARs they are first straightened along their axes. The AR axis is a summary of the AR's geometry, and is defined as the array of grid cells inside the AR that has the largest along-path IVT integral (see Xu et al. (2020b)). By definition, the axis is directed in that it follows the general directions of moisture fluxes within the AR. This enables the identification of the first and last axis points regardless of the

shape, curvature and orientation of the AR. The axis is smoothed by a 10-point moving average to remove small-scale curvatures.

The straightening method is inspired by similar techniques used to straighten images of human chromosomes (e.g. Jahani and Kamaledin Setarehdan (2012); Arora et al. (2017)). Like ARs, chromosomes may appear as straight, bent and at various orientations in their microscope scans. To straighten an AR, slices of a given scalar variable (e.g. IVT[1]) are taken from perpendicular profiles sampled along the AR axis. These equal-length profiles are re-stacked to form a "resample matrix", from which the straightened image is constructed using bi-linear interpolation. More technical details are given in the Appendix, and Fig. 1 gives an example of the straightening process applied on the IVT field of a Northeastern Pacific AR at 2004-Jan-04, 18:00 UTC. The AR boundary is drawn as black contour, and the axis as dotted curve from the starting point S to the end point E (Fig. 1a). It can be seen in Fig. 1b that the axis and profiles form a "fish-bone-like" structure. The straightened image in Fig. 1c is oriented such that the starting point S is on the left hand side and the end point E on the right. Based on the thermal wind relationship, this implies that the bottom side, where the AR width axis is labeled negative, corresponds to the warm side, and the top is the cold side. This orientation is also consistent with the natural coordinate system often used in frontal system studies (e.g. Hoskins and Bretherton (1972); Keyser et al. (1988)). The straightened image is then normalized along the x-axis to give the length-normalized straightened image in Fig. 1d, which now has a fixed dimension and is therefore composite-ready. The binary mask delineating the AR region is also straightened using the same process, and re-discretized to binary using a cut-off value of 0.5.

It can be seen in Fig. 1b that when an AR displays considerable curvature, the profile lines may cross over each other where the AR bends inward, and may create some artifacts in the straightened image. Therefore, we also experimented constructing the profile lines using two curvilinear grids stitched together at the AR axis. An example is given in Fig. S1 in the Supplementary. As a curvilinear grid is qusi-orthogonal, it is immune to the crossing-profiles issue. After interpolation, this creates more natural looking straightened images (Fig. S1c,d), but the broad structure is largely consistent, particularly in the interior of the AR where it is so narrow that virtually no crossing-over happens. After averaging across a large sample, the difference between the two approaches is negligible (two comparisons are given in Fig. S2 and S3). Therefore, the rest of the work is based on results from the "fish-bone" straightening method alone.

2.4 AR straightening method for vector fields

The above straightening method only works for scalar fields as the directional information of a vector field is not preserved during the process. To faithfully straighten a vector field, the azimuthal angle of each profile is first computed, then the original vector direction sampled at each point along the profile is rotated by that amount accordingly, such that the rotated profile aligns with the y-axis in the straightened image. More details on the computation of this rotation angle is given in the Appendix. A nearest-neighbor interpolation is used to interpolate the vector directions onto the target grid, to avoid artifact values across the 0/360 degree joint. Only vector directions are straightened in this manner, the u- and v- components of the vectors, respectively corresponding to the x- and y- dimensions in the straightened image, are recovered from the straightened scalar magnitudes and directions.

Fig. 1c, d also show the straightened **IVT** field of the same AR case. It can be seen that the process achieves a satisfactory retention of the regional circulation patterns. The

[1] in AR researches the term *IVT* is often used to refer to the scalar magnitude |**IVT**| and the vector field **IVT** interchangeably. We will use bold font to emphasis a vector definition in later sections.

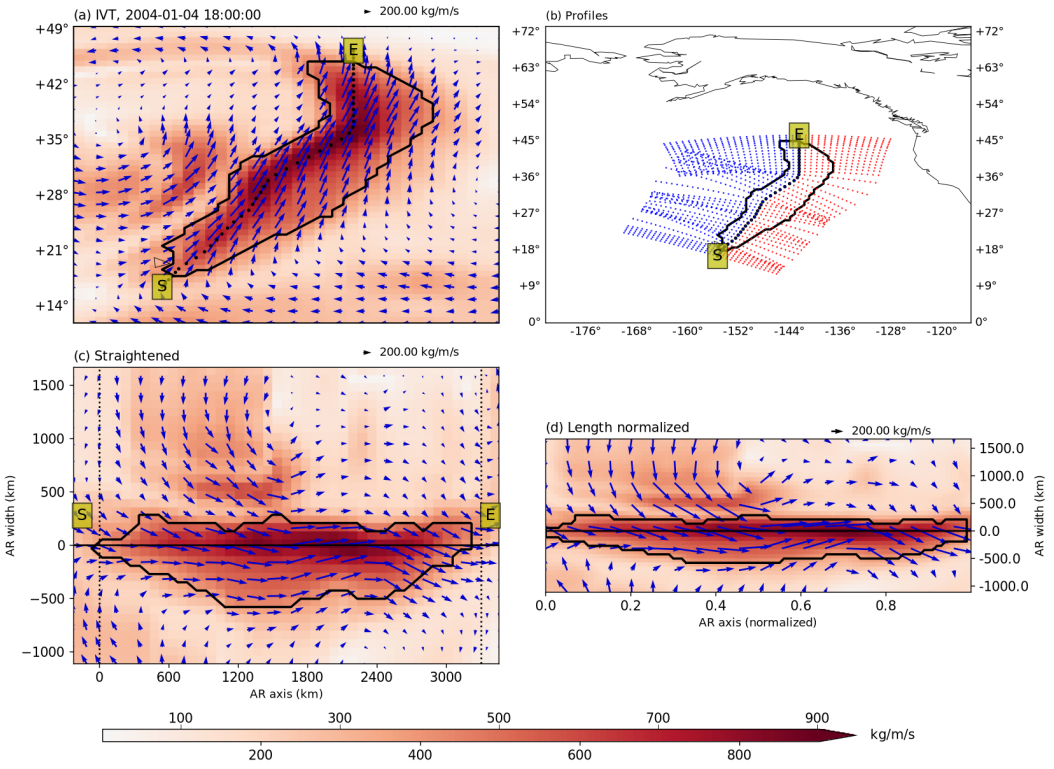

Figure 1. Illustration of the scalar and vector field straightening method. (a) IVT (in $kg/(m\,s)$) distribution of an AR over the Northeastern Pacific at 2004-Jan-04 18 UTC. Magnitudes of IVT are shown as colors, and flux vectors are superimposed on top. The boundary of the AR is drawn as black contour, and the axis is drawn as the dotted curve starting from the starting point S to the end point E. (b) axis and cross sectional profiles of the same AR. Profiles are drawn crossing each axis point perpendicular to the local line segments, with "warm side" profile points drawn in red and "cold side" points in blue. "Warm side" profile limb covers a longitude/latitude distance of 10° with 14 evenly spaced sample points, and "cold side" limb covers a distance of 15° with the same spacing. (c) straightened IVT of the AR. Perpendicular profiles as shown in (b) are re-stacked from the starting point S to the end point E along the x-axis, and scalar IVT is computed from the re-stacked coordinates using bi-linear interpolation. Vector directions are rotated according to the orientation of the profile line. The binary mask of the AR region is also interpolated and re-discretized to binary with a cut-off value of 0.5. (d) straightened IVT of the AR normalized to a fixed shape of 36×100, where 36 is the dimension of the AR width, and 100 the dimension of the AR length.

cyclonic (anti-cyclonic) cell on the cold (warm) side of the AR is well preserved after the straightening, as well as the sharp clockwise turn observed at the southern tip of the AR.

3 Results

3.1 Plane-view composites of ARs and the relationship with extratropical cyclones

North Pacific ARs during 2004-2010 are first detected and tracked. After filtering by a $120°E{-}100°W$ longitudinal range, about 25600 6-hourly AR occurrences (~ 3657 per year) are obtained. Some basic statistics about these ARs are given in Fig. S4. The straightening methods described above are applied on ERA-I data to create composites of various variables. Besides the example given in Fig. 1, four more cases, covering a length span of $\sim 3500 - 6500\,km$, are given in the supplementary Fig. S5-S8. It can be seen that the straightening methods work reasonably well on ARs with a wide range of lengths. There are some minor differences in the straightened composites between different length categories (not shown), however, the basic structures within and around the ARs are consistent. Therefore, for the sake of depicting the general structure of a typical North Pacific AR, it is acceptable to average ARs across the entire length span. However, there are cases when the sizes or locations of the ARs are important. In such situations, further constraints, for instance, specifications on the locations of the starting and ending points of the AR axis, are imposed to obtain a composite with more coherent samples. Such constraints will be specified when explaining relevant analyses.

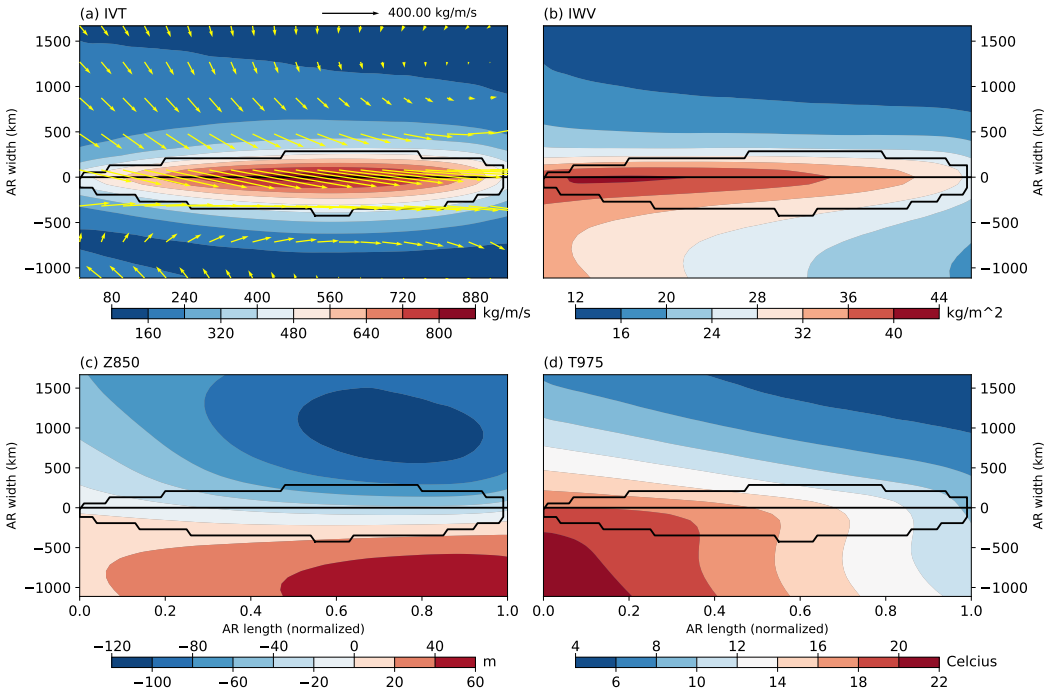

Figure 2. Composites of (a) IVT (magnitude shown as color shading, in $kg/(m\,s)$, and vectors as arrows), (b) IWV (in kg/m^2), (c) geopotential height anomalies at $850\,hPa$ level (in m) and (d) air temperature at $975\,hPa$ level (in Celcius). Composites are created by averaging the straightened fields of North Pacific ARs during the period of 2004-2010. Black contours delineate the averaged boundaries of ARs, and the thin black line the axis of the AR.

Fig. 2 displays the composites of some horizontal fields. It can be seen that the composite of the straightened AR has a shuttle-like shape, with a slightly wider warm side than the cold side, particularly in the middle section of the AR. This is also observed in the case shown in Fig. 1. The straightened **IVT** field is cyclonic on the cold side and anti-cyclonic on the warm side (Fig. 2a). The two circulations converge at the AR region, but with a component towards the warm side. This may explain the observed shape asymmetry that the moisture is "pushed" towards the warm side, and is also consistent with the integrated water vapor (IWV) distribution in that the maximum IWV centers at the axis but skews towards the warm side (Fig. 2b). Unlike the IVT field that has pointed ends, the IWV field is well connected with high IWV levels outside of the AR region on the left side of the straightened image (Fig. 2b). Considering that most Northern Hemisphere ARs have a southwest-northeast orientation, the left end corresponds to the tail of the AR where the atmosphere in lower latitudes has higher vapor contents.

Consistent with the circulation pattern, the $850\,hPa$ geopotential height anomalies ($Z850'$, with respect to the zonal average) feature a low (high) pressure center on the cold (warm) side (Fig. 2c). This dipole pattern was also identified in Z. Zhang et al. (2019), who suggested that the high pressure center is important for ARs that are not associated with a cyclone. Boundary layer air temperature composite shows a warmer "bottom-left" quadrant, a largely horizontal temperature gradient in the x- direction on the warm side of the AR, and a sharper y- direction temperature gradient across the central line (Fig. 2d). This justifies the warm and cold side definitions. The warmer quadrant having higher IWV distribution is also consistent with the Clausius-Clapeyron relationship (e.g. Held and Soden (2006)).

These plane-view composites allude to a typical AR-cyclone relationship: an AR tends to appear around the southeastern edge of a cyclone, aligning along and in front of the cold front[2]. To help depict this AR-cyclone relationship in a geographic map projection, a subset of 300 ARs are randomly selected from those whose starting point falls within the box of $20{-}35°N$, $125{-}140°E$, and ending point the box of $40{-}55°N$, $145{-}160°E$. Composites of IVT, IWV, Z850' and T975 are shown in Fig. S9 in Supplementary. The relationship between the AR and the extratropical cyclone is consistent with the above descriptions. Similar configurations are also observed in composites created from ARs in other longitudinal bands within the North Pacific (not shown). Therefore, this AR-cyclone relationship is a rather consistent feature, suggesting that the trailing AR propagates with the accompanying cyclone. This explains the similarities between the AR track and storm track (Zhu & Newell, 1998; Xu et al., 2020a), and that the former is slightly equatorward in comparison (Mundhenk et al., 2016).

It should be noted that the similar AR-cyclone configuration has been documented by earlier studies from a cyclone-centric perspective (e.g. Dacre et al. (2015, 2019); Z. Zhang et al. (2019)). However, the extent of an AR's width is much smaller than the radius of an extratropical cyclone, and some of the more delicate structures, for instance, the cross-sectional profiles, may be obscured if the AR samples are not accurately aligned up. The next section focuses on such vertical structures.

3.2 Vertical structures of ARs

By applying the same straightening and compositing methods on variables at various vertical levels, the three dimensional structure of a typical AR is reconstructed. The straightened fields are further normalized along the width dimension, by aligning up the AR axes, and interpolating the cold and warm sides separately to a normalized width of 1.0 and -1.25, respectively. The 25% extra warm side width is determined from the

[2] based on this, we use "cross-front" and "along-front" interchangeably with "cross-axis" and "along-axis".

averaged AR mask. Taking the widest cross-section within the middle $25-75\%$ portion of the AR length, the average AR width is about $\sim 800\,km$, which is partitioned into $355\,km$ ($455\,km$) on the cold (warm) side, based on the $1:1.25$ ratio. Note that the average $800\,km$ width is wider than the median width of $500\,km$ as shown in Fig. S4. Aside from the difference between mean and median in a non-Gaussian distribution, this is also because the latter is defined as the "effective width", i.e. the ratio of area over length. The narrower ends of the AR region make the effective width smaller than the width measured at the widest cross-section.

Fig. 3a shows the cross-sectional composite of along-axis moisture fluxes at 50% of the AR length. The moisture flux profile features an asymmetrical dome-like shape, with a flatter base on the warm side. This is consistent with the AR shape asymmetry mentioned previously, and also explains the raised (suppressed) 50, 75 and 90% IVT height levels on the cold (warm) side. These IVT height levels are obtained by integrating the along-axis moisture fluxes from the bottom level up. Therefore, at the core of the AR, 75% of the total IVT is found below $\sim\ 650\,hPa$, and only about 10% above the level of $\sim\ 500\,hPa$. Compared with moisture fluxes, the specific humidity profile does not have as clear lateral boundaries (Fig. 3b), but features a more gradual decline from the center of the AR. However, humidity level also drops much faster on the cold side. The asymmetrical humidity distribution and the tilt of the moisture fluxes towards the cold side are consistent with sounding observations (Ralph et al., 2004, 2017).

The asymmetrical humidity distribution is related to the thermodynamical conditions. Isotherms slope down towards the cold side, with a zone of strong baroclinicity (horizontal temperature gradient $\leq -1K/100\,km$, shown as grey shading in Fig. 3a) on the cold side. The frontal line which is marked by the dash-dotted blue curve in Fig. 3, represents the maximum (negative) temperature gradient at each level, and tilts away from the AR center and towards the upper level low pressure center (Fig. 3c). On one hand, baroclinicity of the system leads to low equivalent potential temperature (Fig. 3d) and low humidity (Fig. 3b) on the cold side. (Due to a faster decreasing rate of temperature with respect to humidity, the relative humidity level is actually higher on the cold side (Fig. 3d)); On the other hand, tightened isotherms across the cold front induce enhanced vertical wind shear via the thermal wind relationship, creating an upper level jet situated above the surface cold front (Fig. 3c). The along-front wind enhancement also extends from the tropopause down to the boundary layer level, where a LLJ is observed (Fig. 3c). It is also interesting to notice that the zero $Z850'$ contour divides the AR cross-section diagonally at 50% of AR length (Fig. 3c). Recall that the geopotential height field tilts westward with height in an extratropical cyclone, required by the hydrostatic balance in a baroclinic wave (Holton & Hakim, 2013). This implies that towards the head of the AR ($>$ 50% length), the upper troposphere above the AR is governed by positive pressure anomalies (not shown).

The pressure, temperature and wind distributions are in accordance with a classical frontal system associated with an extratropical cyclone (e.g. Petterssen (1936); Keyser et al. (1988); Hoskins and Bretherton (1972)). Scale analysis suggests that in the semi-geostrophic theory, the horizontal momentum equation in the frontal system can be approximated by geostrophic balance in the along-front direction ($u = u_g$), but the ageostrophic component becomes non-negligible in the cross-front direction ($v = v_g + v_a$) (K. Browning, 1985; Holton & Hakim, 2013). The existence of ageostrophic winds implies vertical motions, which are shown in Fig. 4, in cross sections at 25, 50 and 75% of the AR length from the equatorward end.

It can bee seen that vertical motion gets increasingly stronger from the tail to the head of the AR (Fig. 4). This is consistent with the relationship between ARs and WCBs, the latter of which have been characterised by both vertical and horizontal motions, in contrast to ARs that are identified solely from horizontal fields (K. Browning, 1985; Cordeira et al., 2013; Ralph et al., 2020). For instance, according to the WCB definition by Wernli

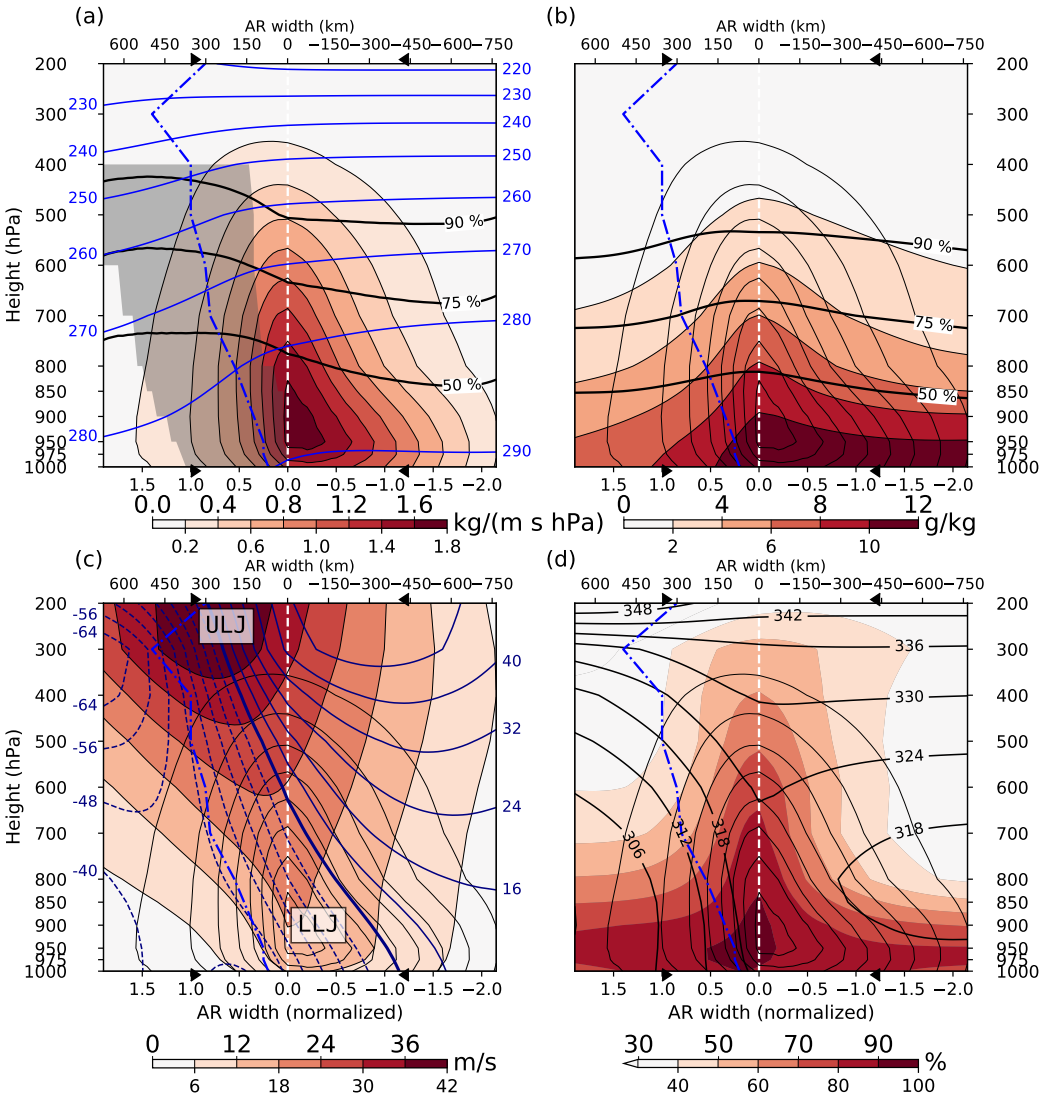

Figure 3. Composite cross-sections of North Pacific ARs. (a) shows the along-axis moisture flux (as color shading, in $kg/(m\,s\,hPa)$), and temperature (as blue contour lines, with an interval of $10\,K$). Thick black contours show the height at which 50, 75 and 90 % of the total IVT are reached, integrating from the ground up. Grey shading represents regions with strong baroclinicity (horizontal temperature gradient $\leq -1K/100\,km$), and the dash-dotted curve denotes the maximum (negative) temperature gradient at each level and represents the position of the cold front. The same IVT contours are also shown in (b), (c) and (d) as thin black contours, and the same front line is recreated in subsequent subplots. The x-axis is the width of the AR, normalized to the average AR width of $800\,km$. Black triangles at the top/bottom x-axes denote the lateral boundaries of the AR, with the cold (warm) side located on the left (right) hand side. (b) IWV profile as color shading, in g/kg. Thick black contours show the height at which 50, 75 and 90 % of the total IWV are reached, integrating from the ground up. (c) along-axis horizontal wind speed as color shading, in m/s. Thick blue contours show the geopotential height anomalies, with an interval of $8\,m$. Negative anomalies are plotted as dashed contours. Locations of the upper-level-jet (ULJ) and low-level-jet (LLJ) are labeled. (d) relative humidity profile as color shading, in %. Thick black contours show the equivalent potential temperature, in K.

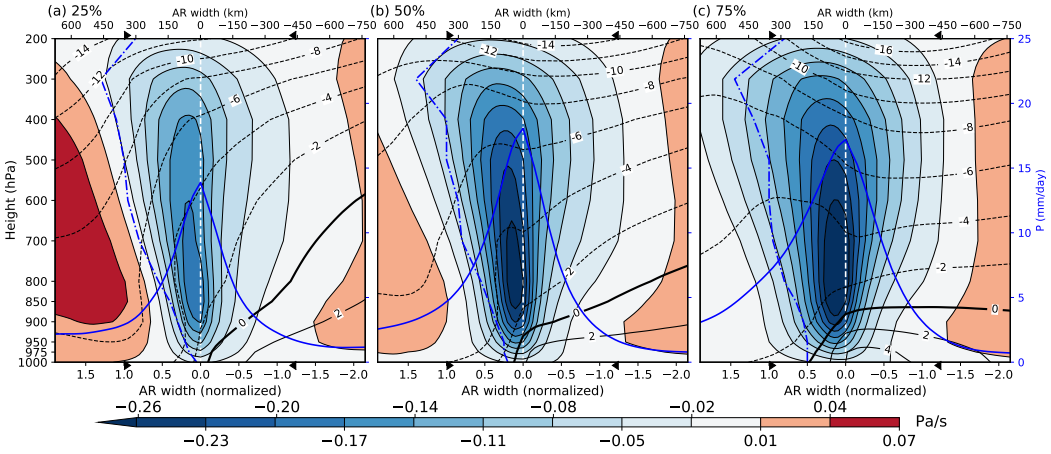

Figure 4. Composite cross-sections at 25 (a), 50 (b) and 75% (c) of the AR length. Color shading shows the pressure velocity (in Pa/s). Black contours show the cross-axis horizontal wind speeds, with an interval of $2\,m/s$. Positive cross-axis wind is directed to the left. Solid blue curves show the precipitation distribution (in mm/day), plotted onto the y-axis on the right. In each subplot, the dash-dotted curve shows locations of minimum negative temperature gradient at each level. The x-axis is width of the AR, normalized to the average width of $800\,km$. Black triangles at the top/bottom x- axes denote the lateral boundaries of the AR, with the cold (warm) side located on the left (right) hand side.

and Davies (1997), a WCB is defined as the region with ascending motions stronger than $600\,hPa$ per $48h$. By this criterion, the WCB is only observed at the end of the AR, beyond the 75% length (not shown).

Accompanied with the concentrated ascending motion is the precipitation distribution that centers at the AR axis but with a flatter tail on the cold side (Fig. 4). This may be explained by the higher relative humidity levels on this side (Fig. 3d), and is also consistent with the so-called "anafront" model that a cold front tends to have upsliding warm air overriding the surface cold front, creating post-frontal precipitation (K. A. Browning & Monk, 1982; K. Browning, 1985; K. A. Browning & Roberts, 1996). The higher rain rates on the cold side is also consistent with a satellite-based composite created from 46 Eastern Pacific ARs (Ralph et al., 2004). Descending motion is found on both flanks of the AR, particularly towards the tail of the AR where the cold front is strongest, forming the cross-frontal secondary circulation with the pre-frontal ascending motions.

Most previous studies focused on the along-axis fluxes/winds in an AR's cross-sections, and few has examined the vertical structure of the cross-axis components. Note that the cross-axis horizontal winds are dominated by winds from the cold side (Fig. 4). Cross-axis warm winds are only found in the bottom section of the troposphere, with decreasing thickness from the tail to the head of the AR. The transition from positive (warm advection) to negative (cold advection) with height is the manifestation of the veering wind, as a result of the thermal wind relationship associated with the warm front. Similarly, across the cold front at the tail half of the AR (Fig. 4a, b), the isotaches have near vertical profiles within $1000-500\,hPa$. Combined with the vertically increasing along-front winds (Fig. 3c), this indicates an anti-clockwise rotation of the cross-frontal winds with height, and is the thermal wind relationship manifest as backing winds. Both of the veering and backing winds help rotate the moisture fluxes from their respective sides to align with the AR axis, thus forming a mechanism that collects moisture from the lat-

eral boundaries of the AR. However, it is worth noting that thermal winds as derived from geostrophic balance do not create any horizontal divergence, unless the Coriolis parameter is not treated as a constant (Benedetto, 1957; Alpert et al., 1995). At frontal scale of a few hundred kilometers, the change of Coriolis parameter is negligible, therefore the strong vertical motion at the AR center can not be explained by the backing and veering winds.

As predicated by the semi-geostrophic theory, ageostrophic winds in the cross-front direction have comparable importance as the geostrophic component. Their relative roles in the AR horizontal moisture fluxes are examined further in the next section.

3.3 Moisture fluxes due to geostrophic and ageostrophic winds

Layered geostrophic and ageostrophic winds and moisture fluxes are first computed before fed into the straightening algorithm, and cross-sectional profiles averaged across the AR length are shown in Fig. 5. Along-axis winds and moisture fluxes are both dominated by the geostrophic component (Fig. 5a,b). Ageostrophic winds show a local minimum at the upper level jet level, extending downward along the front line, pointing in the opposite direction of the geostrophic counterpart (Fig. 5c). This is due to the rearward pointing pressure gradient force created by the westward tilting low pressure center as explained previously. Combined with the low humidity level above the mid-troposphere (Fig. 3b), this offsetting ageostrophic component makes little difference to the along-axis moisture fluxes.

Cross-axis geostrophic winds contribute most of the moisture fluxes into the AR region from the cold side (Fig. 5d, e), while ageostrophic winds, created by the leftward pointing pressure gradient force and surface friction, are responsible for the moisture inputs from the warm side within a more vertically confined region (Fig. 5d, f). These two branches converge towards the AR center, providing the water vapor contents for the along-axis moisture fluxes. Also note that the ageostrophic winds have a local maximum ahead of the surface front, and another in the upper troposphere along the upper level front (Fig. 5f). These two maxima help strengthening the temperature gradients at the lower and upper jet locations, and tilting the frontal zone backwards. Dynamically, they also serve as a forcing term for the along-axis geostrophic wind, according to the momentum equation in the semi-geostrophic framework (Holton & Hakim, 2013): $\frac{Du_g}{Dt} = fv_a$, where u_g is the along-axis geostrophic wind, v_a the cross-axis ageostrophic wind, and f the Coriolis parameter. On the other hand, geostrophic winds contribute a much greater amount of moisture from the cold side (Fig. 5e, see also analyses in later section). The lower humidity level on the cold side is over compensated by a much stronger cross-frontal geostrophic wind. Furthermore, cold geostrophic advection in the mid-troposphere and warm ageostrophic advection in the boundary layer help reduce static stability, creating a zone of neutral moist static stability at the core of the AR (Fig. 3d), consistent with sounding observations (Ralph et al., 2005; Neiman et al., 2013). Diabatic processes fostered by the near saturated and ascending air are likely to contribute significantly as well. In summary, both geostrophic and ageostrophic winds make indispensable thermodynamic and dynamic contributions to the high moisture fluxes of ARs. Consequently, their evolutionary changes are likely to get reflected in the changes of the AR moisture fluxes as well. This subject is explored in the next section.

3.4 Evolutionary changes of AR moisture fluxes

The same AR entity is first tracked through space and time using the method introduced in Xu et al. (2020b). Only tracks lasting for at least 24 hours are retained. Daily composites from genesis (0H) up to day-5 (120H), which is roughly the 80% percentile in the duration distribution (see Fig. S10), are shown in Fig. 6. All composites are the

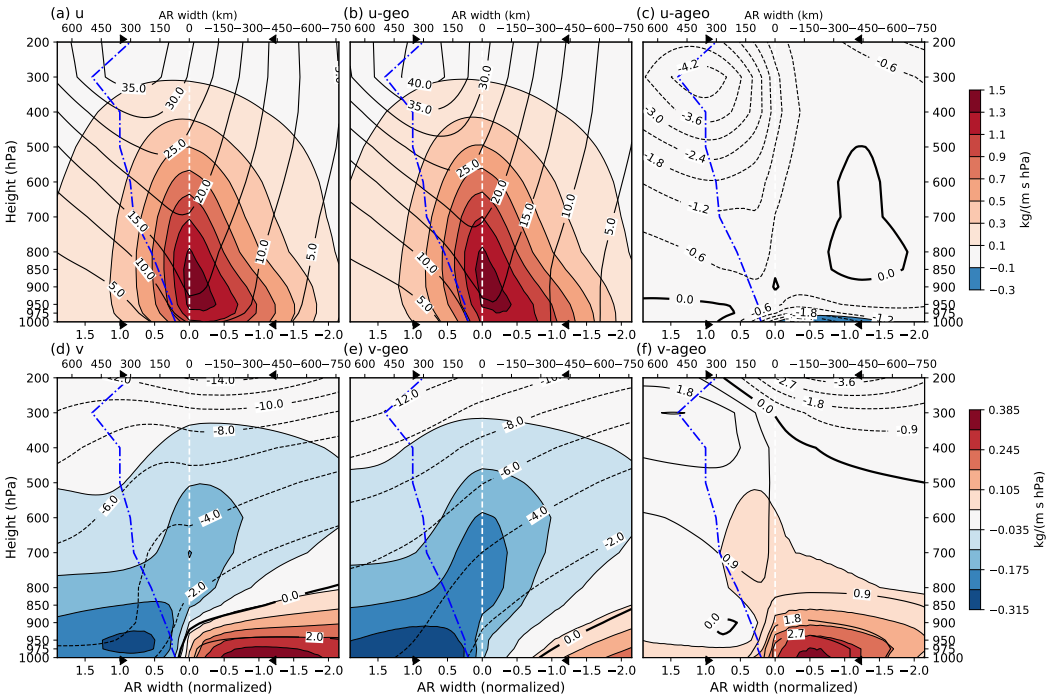

Figure 5. Composites of geostrophic and ageostrophic components of the along-axis (top row) and cross-axis (bottom row) moisture fluxes and winds. (a) the along-axis moisture flux (color shading, in $kg/(m\,s\,hPa)$) and along-axis wind speeds (black contours, in m/s), and their respective geostrophic components in (b) and ageostrophic components in (c). (d) the cross-axis moisture flux (color shading, in $kg/(m\,s\,hPa)$) and cross-axis wind (black contour, in m/s), and their respective geographic component in (e) and ageostrophic components in (f). All results are the average across the entire AR length.

averages across the entire AR length. Considering their dominant role, only the moisture fluxes by geostrophic winds are shown for the along-axis direction.

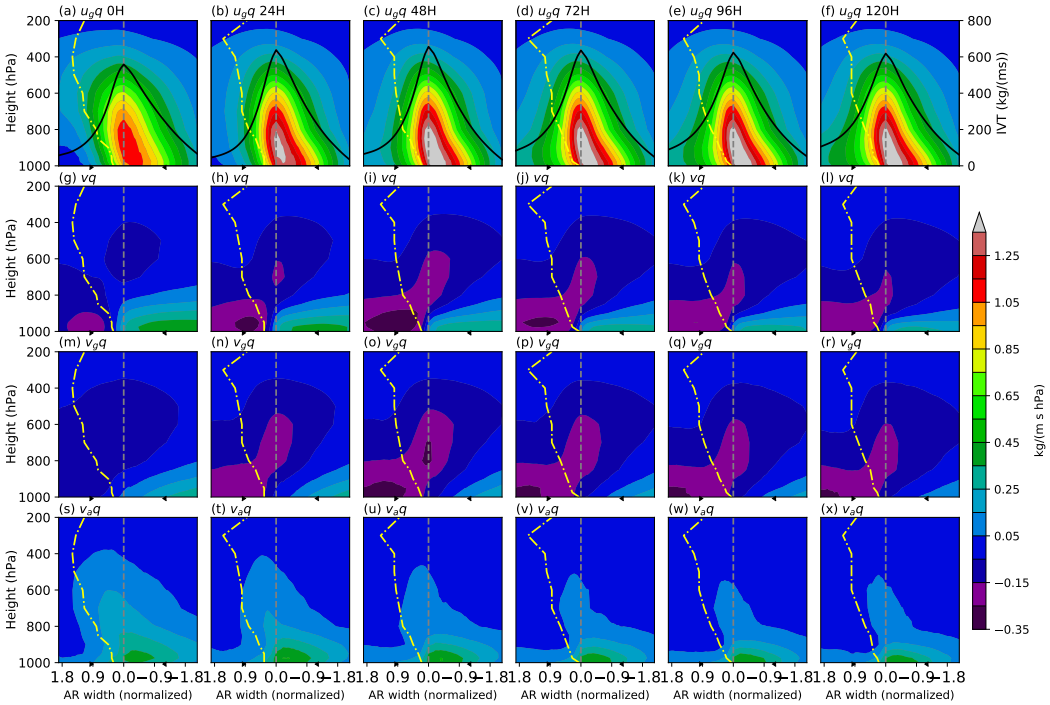

Figure 6. Composite cross-sectional geostrophic and ageostrophic moisture fluxes (color shading, in $kg/(m\,s\,hPa)$). From left to right, columns are 0, 24, 48, 72, 96 and 120H after the first detection of the AR track. Top row shows the along-axis geostrophic moisture flux. Solid black curve is the IVT profile (in $Kg/(m\,s)$), plotted onto the y-axis on the right hand side. Second row shows the total cross-axis fluxes, which are decomposed into the geostrophic component in the third row, and the ageostrophic component in the last row. In all subplots, the yellow dash-dot curve denotes the location of the cold front, and black triangles at the bottom edge denote the lateral boundary the AR. All profiles are averaged across the entire AR length.

It can be seen that ARs tend to reach their peak IVT intensity about two days after genesis (top row in Fig. 6), followed by a gradual decline afterwards. This is in phase with the variation of cold side moisture fluxes (2nd row in Fig. 6), which are mostly contributed by the geostrophic component (3rd row in Fig. 6). Moisture fluxes from the warm side, on the other hand, show a gradual retreat from the genesis time (2nd row in Fig. 6). This is a result of weakening geostrophic (3rd row in Fig. 6) and ageostrophic (4th row in Fig. 6) fluxes from the warm side. However, the local maximum of ageostrophic fluxes in front of the surface cold front persists throughout the process. The above evolutionary changes are further validated by time series of the moisture fluxes given in Fig. 7a. Vertical integral of the along-axis geostrophic flux ($< u_gq >$) reaches its peak value about 48 hours after genesis, in sync with the variation of cold side cross-axis geostrophic flux ($- < v_gq >_c$). Warm side cross-axis ageostrophic flux ($< v_aq >_w$) makes a bigger contribution during first 24 hours, serving as the dominant factor for lateral moisture inputs during genesis, but gets surpassed by the cold side counterpart and continues to weaken afterwards.

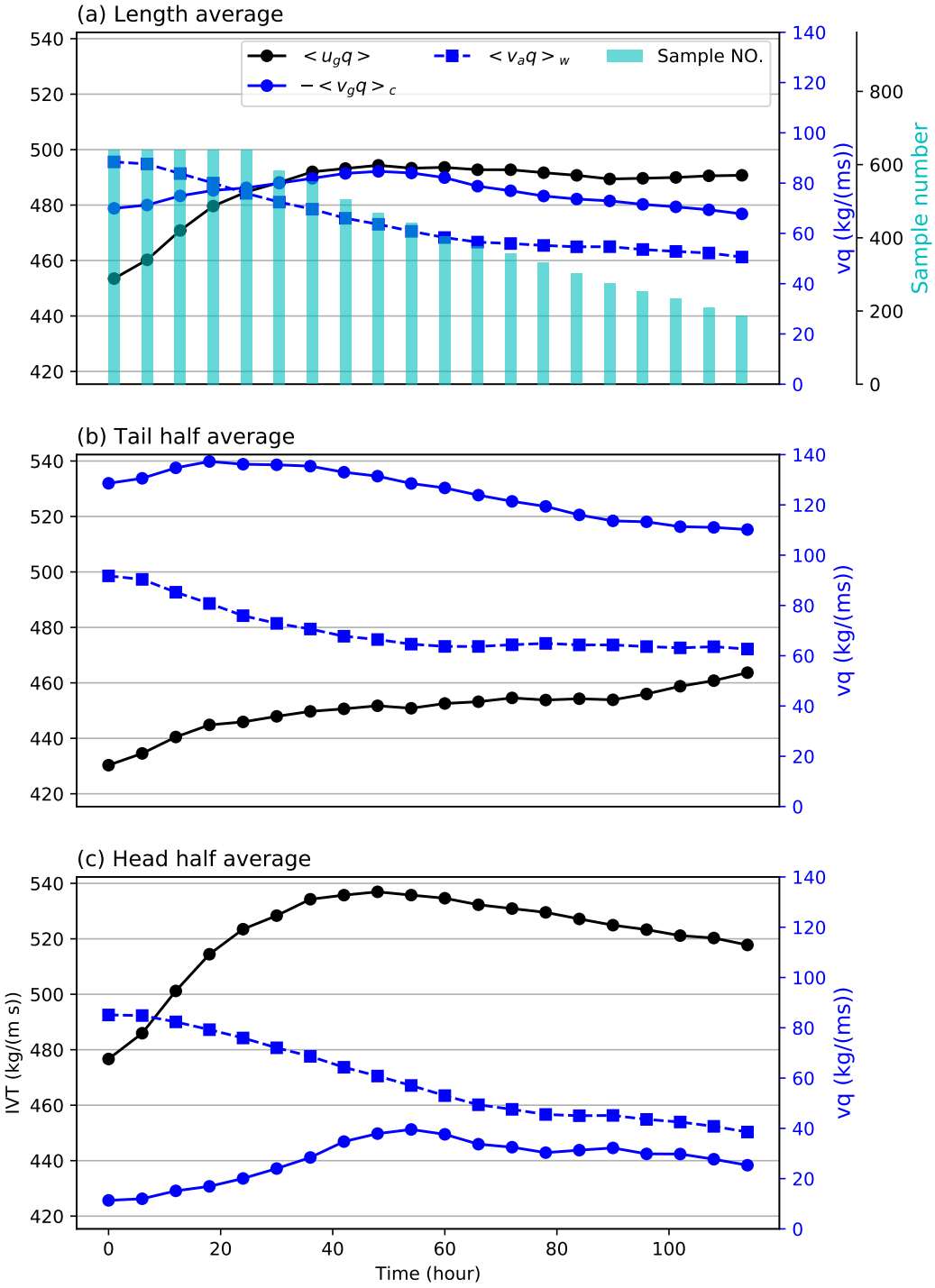

Figure 7. Time series of vertical integrals of moisture fluxes (in $kg/(ms)$) following the evolution of ARs. Black curve shows the along-axis moisture flux by geostrophic winds ($< u_g q >$), solid blue curve shows the negative of cross-axis geostrophic moisture flux from the cold side ($- < v_g q >_c$), and dashed curve the cross-axis ageostrophic moisture flux from the warm side ($< v_a q >_w$). The two blue curves are plotted onto the y-axis on the right hand side. (a) shows the averages across the entire AR length, (b) the averages of the tail half (0 − 50% length) of the ARs, and (c) the averages of the head half (50 − 100% length). The number of AR samples in each 6-hourly time step are shown as cyan bars in (a), plotted onto the 2nd y-axis on the right.

Note that longer-lasting ARs get progressively rarer, as shown in Fig. 7a, and the above evolutionary analyses do not distinguish ARs with possibly different life spans. To investigate these effects, we further split the AR tracks into a short duration group where ARs last for $24-72$ hours, and a long duration group where ARs last for longer than 72 hours. The chosen 72 hour threshold is slightly above the median of the duration distribution (see Fig. S10). Time series of moisture fluxes in these two groups are given in Fig. S11 in the Supplementary. It can be seen that ARs with short and long durations share similar evolutionary changes during the first 48 hours that are consistent with the above analyses (with the exception that ageostrophic moisture fluxes from the warm side get surpassed by the cold side geostrophic component even sooner in the short duration group).

After the peak intensity time, moisture fluxes from both sides weaken with the along-axis fluxes, suggesting a possible relationship between the lateral moisture inputs and the intensity of the AR IVT. However, IVT can also be affected by changes in the along-axis winds. To further distinguish the dynamical and thermodynamical contributions, changes in the along-axis geostrophic moisture fluxes at different stages are decomposed into a dynamical component ($q\Delta u_g$), a thermodynamical component ($u_g\Delta q$), and a covariance term ($\Delta(u_g q)$), where Δ denotes a time difference from 0H. The results are given in Fig. 8. Compared with 0H, along-axis geostrophic moisture fluxes get stronger within a narrow band along the AR axis, and within a layer below $800\,hPa$ level behind the front (Fig. 8a-e). This is a combined effect from the dynamical component as the primary intensification mechanism ($q\Delta u_g$, 2nd row in Fig. 8), and the thermodynamical component as a partially offsetting mechanism ($u_g\Delta q$, 3rd row in Fig. 8).

The changes in the along-axis geostrophic winds (Fig. 8f-j) are largely consistent with the changes in cross-frontal pressure gradients ($\frac{g}{f}\Delta(\frac{\partial Z}{\partial x})$) (Fig. 8a-e). When multiplied with a vertically decreasing humidity distribution, the resultant changes in geostrophic moisture fluxes are confined to the mid-lower troposphere. On the other hand, moisture level drops at both sides of the AR, and to a lesser extent, along the AR axis (Fig. 8k-o). Largest humidity decrease is found below $\sim\ 700\,hPa$ behind the front, consistent with Dacre et al. (2015). When multiplied with the strong jet wind speeds, this decrease largely offsets the dynamical intensification effects ahead of the front in the mid-troposphere. The greater extents of humidity decreases at the lateral boundaries compared with the core region also reflect the convergence of moisture into the AR interior, and the overall decrease of humidity a net export of water vapor within the AR region. Lastly, contribution made by the covariance term ($\Delta u_g \Delta q$, Fig. 8p-t) is much weaker, but tend to offset the along-axis moisture fluxes on the cold side.

A similar decomposition is performed on the cross-axis moisture fluxes, but separately for geostrophic and ageostrophic components. Only the significant terms are shown in Fig. S12 in the Supplementary. The results, combined with the above along-axis counterparts, suggest that the evolutionary changes of cold and warm side moisture fluxes as shown in Fig. 6 are mostly due to the dynamical terms of the geo- and ageostrophic winds, with some offsetting effects from the thermodynamical terms.

To summarize the evolutionary changes: ARs tend to experience an early IVT intensification period during the first two days after genesis, dynamically powered by the intensifying along-axis geostrophic winds. Strong moisture fluxes from the warm sector and the rapidly strengthening fluxes from the cold side help provide extra moisture, however, they are not enough to offset the dropping level of moisture within the AR domain. Consequently, although the along-axis geostrophic winds remain as strong in later stages of AR development, reduced moisture level becomes an increasingly important factor. Meanwhile, moisture supplies from the cold (warm) side also drop, largely due to the weakening cross-frontal geostrophic (ageostrophic) winds. In essence, water vapor content becomes a limiting factor for further IVT intensification.

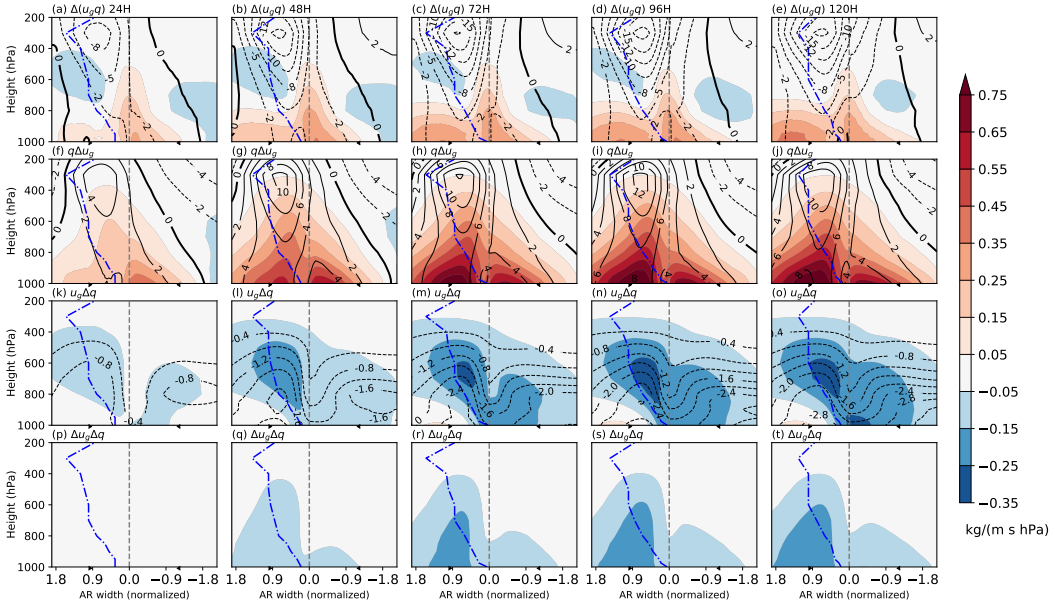

Figure 8. Changes in the along-axis moisture fluxes during AR evolution. Columns are the differences between 24, 48, 72, 96 and 120H from 0H. First row shows the differences of geostrophic moisture fluxes ($\Delta(u_g q)$) as color shading, in $kg/(m\,s\,hPa)$. Black contours show the changes in the cross-axis pressure gradient, scaled by a constant factor of $g/f_0 = 10/10^{-4} m/s$ to a unit of m/s. Second row shows the changes contributed by the dynamical term ($q\Delta u_g$) as color shading, in $kg/(m\,s\,hPa)$. Black contours show the changes in the along-axis geostrophic winds, in m/s. Third row shows the changes contributed by the thermodynamical term ($u_g \Delta q$) as color, with the changes in humidity itself drawn as black contours, in g/kg. The last row shows the contribution made by the covariance term ($\Delta u_g \Delta q$). In all subplots, the blue dash-dot curve denotes the location of the cold front, and black triangles at the bottom edge denote the lateral boundary the AR. All profiles are averaged across the entire AR length.

The above analyses also reveal that during the majority of AR life cycle, moisture fluxes within the AR region are directed from the cold side. This is also observed in the plane-view IVT composite in Fig. 2a and the cross-sections in Fig. 5. However, the lateral flux distribution is not axially symmetric along the axis. This is illustrated by the time series in Fig. 7b,c that, a greater amount of moisture fluxes are directed into the AR domain from the cold side in the tail half of the AR, and the opposite is observed in the head half, but with a smaller difference between the two sides. Therefore, the lateral moisture influx averaged across the course of the AR is dominated by that from the cold side, and complex patterns of moisture fluxes exist within the AR domain.

Furthermore, Dacre et al. (2019) previously proposed a "feeder airstream" mechanism and suggested that fluxes from the warm sector are the primary moisture source for the intensification of ARs. This discrepancy may be caused by the different reference systems used in the analyses: a cyclone-relative frame of reference in their study, and an Earth-relative frame of reference in this work so far. The next section gives a closer look at the spatial patterns of AR moisture transports and compare them in these two frames of reference.

3.5 AR Moisture transports in Earth- and AR-relative frames of reference

The typical moisture transports pattern by an AR in an *Earth-relative* frame of reference is represented by the cross-boundary moisture fluxes across the bounding box of the straightened AR, averaged across the entire evolution stage (Fig. 9). Moisture fluxes across the air-sea interface are approximated by vertical fluxes at the $1000\,hPa$ level, and the top "lid" has been omitted for its low humidity level. Moisture fluxes across the four vertical sides, i.e. the cold side (Fc), warm side (Fw), rear side (Fw) and frontal side (Ff) are displayed as an unfolded box (see Fig. 9b for a schematic). Positive fluxes are defined as outward and vice versa. Side-integrated moisture fluxes are computed using an average AR width of $800\,km$ and an average length of $3500\,km$. The total precipitation within the bounding box is also integrated and scaled to a unit of $10^8 kg/s$, as an extra moisture output term.

It can be seen that the frontal and rear sides have similar patterns of cross-boundary fluxes (Fig. 9e, c), but with stronger magnitude in the former (2.5 versus $-2.1\times10^8 kg/s$, Fig. 9g). This is consistent with the head-tail half differences shown in Fig. 7b,c, and implies a "tunneling-out" effect of moisture along the course of the AR. The largest moisture input term is the geostrophic fluxes from the cold side, with a stronger magnitude than that from the rear side, although the moisture flux intensities are much weaker. Ageostrophic fluxes pointing towards the cold side account for a small offset. The relationship is reversed on the warm side: geostrophic winds create a $\sim 1.0\times10^8 kg/s$ moisture output, which is overcompensated by a slightly stronger ageostrophic moisture input, reflecting the same head-tail distinction mentioned above. Vertical fluxes from the bottom is much smaller compared with other four sides, and precipitation serves as the largest output term with a magnitude of $\sim\ 2.7\times10^8 kg/s$. Overall, the atmosphere is slightly dried out at a rate of $\sim 0.2\times10^8 kg/s$ due to the existence of the AR.

Note that the vertical side integration involves the multiplication of horizontal moisture flux with area. The straightening algorithm does a satisfactory job in preserving scalar and vector fields, however, shape distortion is inevitable, and might affect the areal integration. To help validate the results and evaluate the possible effects from shape distortion, the cross-boundary flux analysis is repeated on a subset of ARs whose starting and ending points fall into specific regions. For the central North Pacific sector, the starting box is chosen to be $20-35°N, 150-165°E$, and the ending box $40-55°N, 170-185°E$. The samples are further filtered by the length and average axis curvature (see Appendix for definition) both being within one standard deviation around their respec-

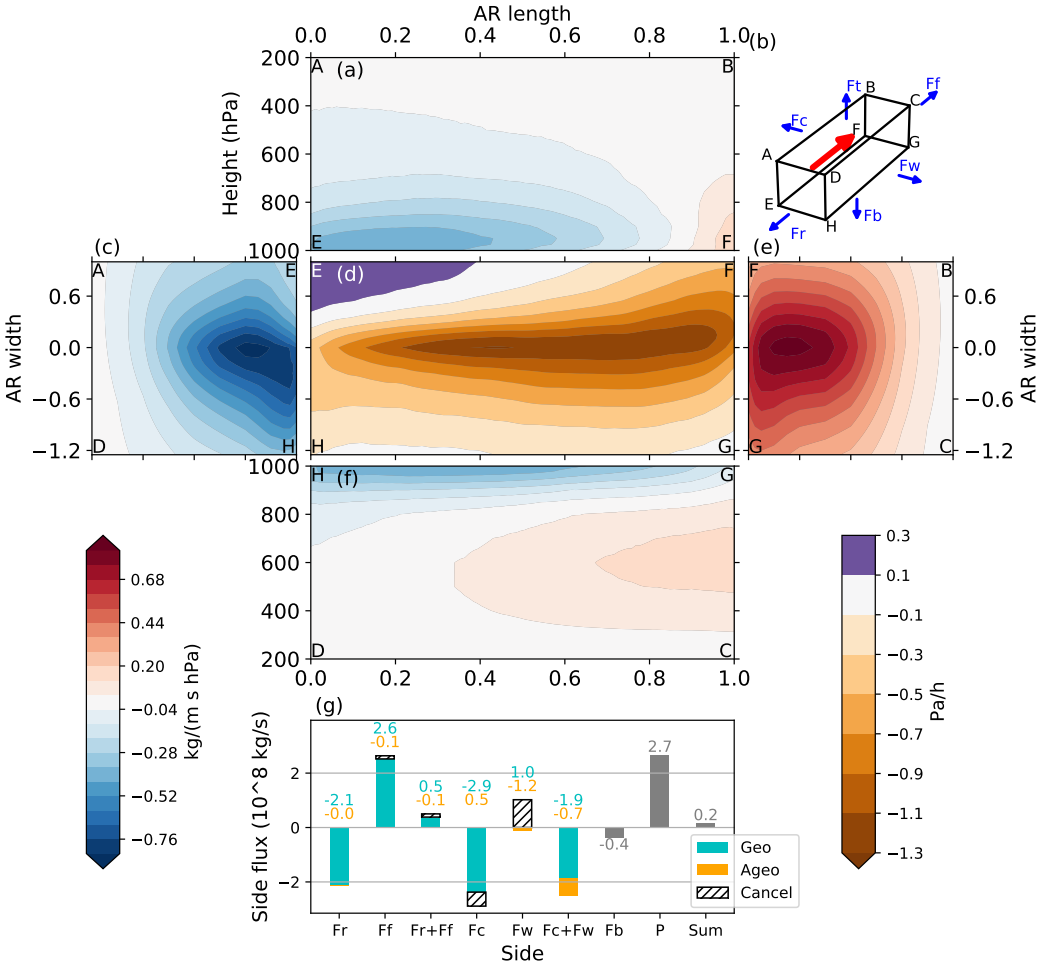

Figure 9. Moisture fluxes across the bounding box of a typical North Pacific AR. A 3D schematic showing the bounding box is given in (b), and the red arrow shows the mean IVT direction. The moisture fluxes across the cold side (F_c) is given in (a), the rear side (F_r) in (c), bottom side (F_b) in (d), frontal side (F_f) in (e), and the warm side (F_w) in (f). Vertices of the bounding box are labeled at the corner of each side, for instance, the side $ABFE$ is the one facing the cold front, whose contour is given in (a). Note that the four vertical sides share the colorbar at the bottom-left corner, in units of $kg/(m\,s\,hPa)$, and the bottom side uses a separate colorbar at the bottom right, in units of Pa/h. Positive contours denote outward moisture fluxes, and vice versa. (g) shows the side-integrated outward moisture fluxes across the five sides, in $10^8 kg/s$. Fluxes due to geostrophic winds are plotted in cyan, and those by ageostrophic winds in orange. If the ageostrophic component has an opposite sign as the geostrophic counterpart, the geostrophic part that gets offset is shown as hatched. Also shown are the sum of the rear and frontal sides ($Fr + Ff$), the sum of the cold and warm sides ($Fc + Fw$), the areal-integrated precipitation (P, in $10^8 kg/s$), and the sum of all five sides plus precipitation.

tive means. These requirements should guarantee a reasonable shape and location coherence of the AR samples in the composite. The results are given in Fig. S13 in the Supplementary. Another composite in the western North Pacific (Fig. S14), and one in the eastern North Pacific are also created (Fig. S15). In all sector-specific results, the relative importance of fluxes from different directions is consistent with the composite taking into all North Pacific ARs: moisture export by precipitation is much stronger than the input by evaporation, consistent with Cordeira et al. (2013). The most important moisture input comes from the cold side geostrophic fluxes, concentrated on the tail half of the AR. Large cancellation is observed between inward and outward moisture fluxes on the warm side. And the sum of the frontal and rear side fluxes creates a small net moisture deficit, indicating the "tunneling out" effect of the AR.

However, the lateral moisture fluxes are expected to be different when changing from an Earth-relative to AR-relative frame of reference. To illustrate this, the translation velocity ($\mathbf{V_t}$) of an AR is first quantified using a centered difference scheme on the 6-hourly AR locations, which are approximated by the IVT-weighted centroids. Then "effective winds" (Sohn & Park, 2010; Zahn & Allan, 2011) of $\mathbf{IVT}$ are computed as: $\mathbf{V_e} \equiv \mathbf{IVT}/IWV$. The AR-relative effective winds are defined as $\mathbf{V_r} \equiv \mathbf{V_e} - \mathbf{V_t}$, and AR-relative $\mathbf{IVT}$ as $\mathbf{V_r} \cdot IWV$. A composite is created using ARs whose starting point falls within the box of $20-35°N, 135-150°E$, and end point in the box of $40-55°N, 155-170°E$. The results are shown in Fig. 10.

It can be seen that the effective winds within ARs are largely in geostrophic balance and follow the $Z850'$ contours (Fig. 10a). When multiplied with IWV, this creates the shuttle-like IVT distribution in the straightened view (Fig. 10b). The average AR translation velocity is northeastward, more or less the same as the propagation speed of the extratropical cyclone (Fig. 10c). However, in the AR-relative frame of reference, effective winds change into easterlies (Fig. 10e), indicating a faster AR movement speed than the low level winds, consistent with Dacre et al. (2019). These easterly AR-relative horizontal winds bring in moisture from the warm side of the cyclone, and diverge at the eastern boundary of the AR into two branches (Fig. 10e, f). One branch steers northward wrapping around the low pressure center, and the other branch southwestward towards the tail of the AR. This northward branch enters the WCB, and the diverging easterly flow is the "feeder-airstream" proposed by Dacre et al. (2019).

Moisture fluxes associated with the translational and relative velocities also contribute differently to the total AR IVT. Fig. 10 shows that the translational winds contribute most of the total IVT in the tail half of the AR, across the rear and cold sides. Based on the previous analyses, this corresponds to the largely geostrophic moisture advections that are carried along by the moving AR-cyclone couple. The northward branch of the "feeder-airtream", on the other hand, makes bigger contributions within the head half of the AR, representing the newly collected moisture by the fast moving AR.

It is worth noting a few precautions when making a direct comparison with the AR formation mechanism proposed by Dacre et al. (2019). Firstly, the $1500\,km$ radius in their cyclone-centric composites does not cover the full extent of the trailing AR. Secondly, the similarity between the cyclone movement speed, AR movement speed and low-level wind speed makes the cyclone- or AR- relative wind estimates very sensitive to their differences. Lastly, the time period examined by Dacre et al. (2019) is centered around the maximum cyclone intensity and is likely to emphasize more on the early development stage of ARs, while no time period preference is enforced in the composite in Fig. 10. Despite these precautions, the broad structure of the AR-relative moisture transports is in accordance with the argument that the "feeder-airstream" is an important moisture source for the AR-cyclone couple: the northward branch of "feeder-airtream" forms the head half of the AR, and the rearward branch advects warm, moist air from the warm sector towards the AR, thus preconditioning the atmosphere with vapor contents that would soon be collected by the propagating AR. The warm side contribution is also found

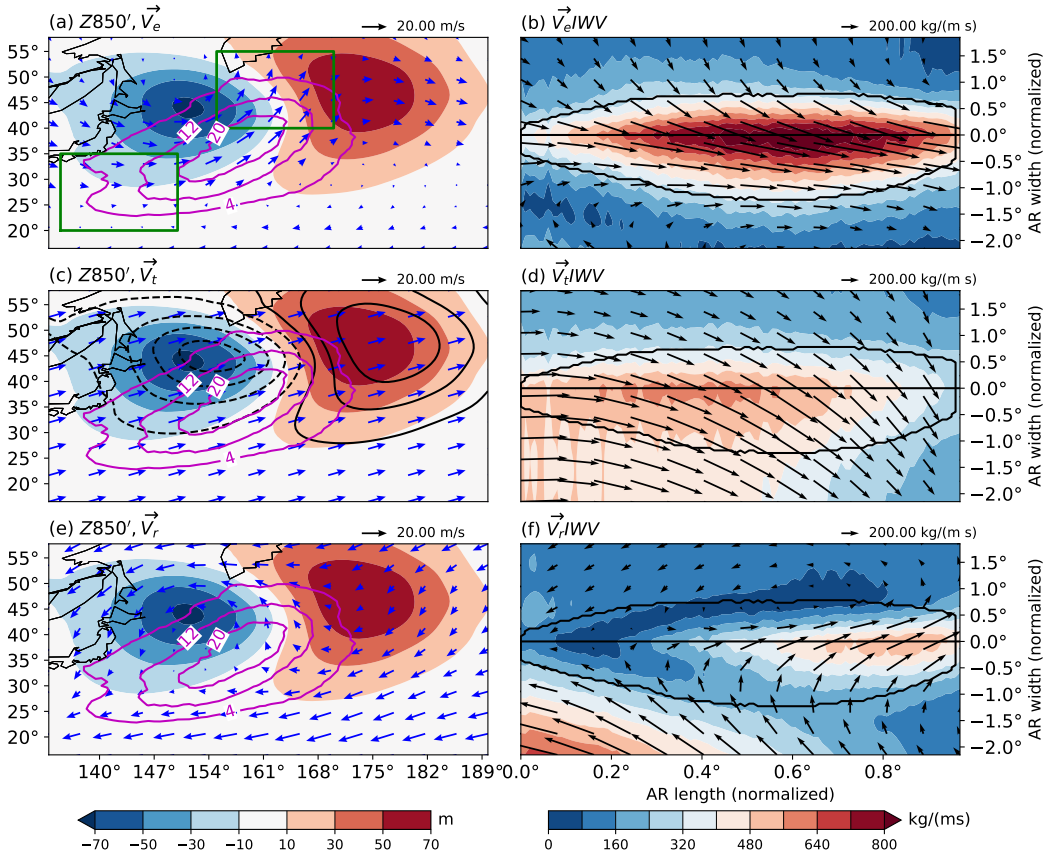

Figure 10. Left column shows the composite of 850 hPa geopotential height anomalies ($Z850'$) as color shading (in m), and AR occurrences as pink contours (in number of ARs per year). The composite is created by selecting ARs whose starting point falls within the box of $20 - 35°N, 135 - 150°E$, and end point the box of $40 - 55°N, 155 - 170°E$. The two boxes are plotted as green rectangles in (a). Black contours in (c) show the $Z850'$ distribution 6-hours later, to indicate the movement of the cyclone. Blue vectors show the effective winds $\mathbf{V_e}$ in (a), the mean translation velocity $\mathbf{V_t}$ of the ARs in (c), and the AR-relative effectives winds $\mathbf{V_r}$ in (e). Right column shows the straightened IVT of the selected ARs as color shading (in $kg/(m\,s)$). (b) shows the effective winds as black arrows and the IVT attributed to that $\vec{V}_e IWV$. (d) and (f) show the corresponding components due to the mean translation velocity $\vec{V}_t IWV$ and AR-relative effectives winds $\vec{V}_r IWV$, respectively.

to be strongest during the first 24 hours after genesis (will only be stronger once transformed into the AR-relative frame of reference), and is therefore consistent with the peak cyclone intensity timing adopted by Dacre et al. (2019). Additionally, analyses in this work also highlight the importance of the geostrophic moisture advection in the tail half of the AR. This component captures a large portion of the overall AR moisture transport during the majority of AR life cycle, and represents the moisture transport carried along the propagating AR-cyclone couple.

4 Conclusions and discussions

In this work, we developed a method to straighten the scalar and vector fields associated with an AR into a composite-ready form, thus making the otherwise cumbersome AR composite analyses from gridded atmospheric data more practically achievable. By applying the straightening methods on different vertical levels on a large sample size, a three dimensional composite of a typical North Pacific AR is reconstructed. The results depict a typical AR-cyclone relationship consistent with previous findings: a North Pacific AR is typically found within the southeastern quadrant of an extratropical cyclone, aligning along and in front of the surface cold front.

The straightening method allows for a more accurate depiction of an AR's cross-sections, many aspects of which can be verified by sounding- and satellite-based observations. Both the IVT and IWV profiles display an asymmetrical distribution about the AR axis. A backward tilting frontal zone is observed, and a low level jet is found ahead of the surface front, within of core of the AR. The AR core also collocates with a zone of high relative humidity, neutral moist static stability and concentrated vertical motions.

ARs have an important dynamical feature that they stride across two major length scales: synoptic scale in the along-axis direction where geostrophic balance dominates, and meso-scale in the cross-axis direction where ageostrophic processes are of equal importance (K. Browning, 1985; Holton & Hakim, 2013; Cordeira et al., 2013). At meso-scale, a thermally direct cross-sectional secondary circulation is observed, with strong ascendings in front of the surface cold front and descendings behind it, consistent with the semi-geostrophic theory. Boundary layer ageostrophic winds help converge moisture from the warm sector, and also help maintain the strong temperature gradients across the front. As a result, the thermal wind balance tends to be interrupted, and along-front winds intensified by the Coriolis force as a restoring mechanism, contributing to the strong AR IVT. These highlight the close relationship between AR development and frontogenesis processes.

During the first two days of AR life cycle, the moisture influx from the lateral boundaries, together with the strengthening along-axis geostrophic winds, lead to the peak IVT intensities during the life time of the AR. After about 48 hours since genesis, the lateral moisture influx weakens, and the AR IVT intensity starts to decline as well. Dynamical-thermodynamical analyses indicate that although the along-axis winds remain as strong, moisture level within the AR region drops and becomes a limiting factor for further IVT intensification. The lower humidity levels at higher latitudes, into which most ARs propagate, may also contribute. On the other hand, the atmosphere is dried out by the residing AR, reflecting AR's role as an effective poleward moisture transport mechanism (Zhu & Newell, 1998).

From an Earth-relative perspective, fluxes from the cold side form the primary moisture source for the atmosphere resided by an AR, replenishing the net moisture loss along the course of the AR. This is also the primary vapor source that offsets the deleterious effect from precipitation, consistent with Cordeira et al. (2013). Moisture advection from the warm side is mostly attributed to ageostrophic winds confined within the boundary layer. The backing and veering winds associated with their respective fronts help rotate

the uplifted moisture fluxes to align with the AR axis, thus forming a moisture aggregation mechanism that gathers moisture from the lateral boundaries. Recall that the AR is aligned along the cold front, and the cold side cross-frontal moisture fluxes are mostly geostrophic. Therefore, the cold side moisture input is fundamentally created by the baroclinicity of the system in that the angle formed by the isoterms and isobars give rise to the cold side moisture influx.

The AR-relative moisture transport pattern is consistent with the "feeder-airstream" concept proposed by Dacre et al. (2019). This downstream easterly flow diverges into two branches, with the northward branch entering the head of the AR. The southward branch does not directly form the body of the AR, but preconditions the immediate downstream atmosphere with more vapor contents. The component that bridges the Earth- and AR-relative moisture transports is the moisture fluxes by translational winds. In the tail half of the AR, total AR IVT is mostly contributed by translational moisture fluxes, representing the largely geostrophic moisture advections carried along by the propagating AR/cyclone couple. In the head half of the AR, total AR IVT is mostly contributed by the northward branch of the AR-relative "feeder-airstream", suggesting that the eastward propagating AR-cyclone couple is "claiming" more moist-loaded atmospheric territory, "harvesting" more vapor contents along the way. Note that it does not necessarily mean that the water vapor has been staying still in the downstream atmosphere, waiting to be collected. They may have gone through a long tropical or mid-latitude trajectory before coming into the AR (Bao et al., 2006).

The divergent movement of the AR-relative "feeder-airstream" and the swift directional transition within the course of an AR are related to the similarity between the AR-cyclone movement speed and the speed of low level winds. This sensitive response to AR-cyclone movement speed may have some important morphological implications on ARs. For instance, the diverging flows stretches the AR along its axis, and may serve as an AR length growth mechanism. This stretching effect works on the AR continuously, and may explain the delayed timing of peak length compared to peak IVT intensity as observed in Xu et al. (2020a). It is also observed that the maximum precipitation center within the AR composite tends to shift rearward as the AR propagates from western into central North Pacific (not shown). This may not be an evolution-related feature, because ARs originating from central Pacific have their precipitation center already shifted. Instead, we speculate that this is due to the longitudinal differences in the cyclone movement speed. Cyclones (and therefore their accompanying ARs) tend to travel faster within the mid-latitude jet streams (Hoskins & Hodges, 2002)). Based on the pattern in Fig. 10, the AR-relative moisture fluxes become more northeasterly with a faster translation speed, creating a longer northward branch of the "feeder-airstream" and a longer WCB. However, further analyses are required to validate this hypothesis.

Lastly, this work has a number of limitations. The AR composites take in all AR samples without any discriminations on seasons, latitudes, lengths, orientations and shapes etc.. Therefore, the results only reflect the general structure of a North Pacific AR, with considerable case-to-case differences masked out. Moreover, the AR-cyclone model is also highly simplified and generalized, and the true picture in particular cases may be considerably more complex. For instance, it is common for an extratropical cyclone to have more than one cold fronts (e.g. Ralph et al. (2004)), and it is also possible for an AR to be associated with two cyclones (Sodemann & Stohl, 2013; Dacre et al., 2019), or none at all (Z. Zhang et al., 2019). ARs can also deviate away from the cyclonic curvature as depicted in the typical AR-cyclone composite, and have straight, or anti-cyclonic shapes, possibaly affected by the interactions with the jet streams (Cordeira et al., 2013), or different types of Rossby wave breaking (Ralph et al., 2020). The meso-scale frontal structure also comes with various configurations (K. A. Browning & Monk, 1982; K. Browning, 1985; K. A. Browning & Roberts, 1996; Schultz et al., 1998). We did not quantitatively examine the frontogenesis processes and the interactions with ARs, nor the adi-

abatic processes associated with the pre-frontal ascendings, which may play a crucial role in the maintenance of ARs. Due to shape distortions involved in the straightening process, the bounding box moisture flux analysis should only be regarded as a qualitative estimate of the relative importance of moisture fluxes from different directions, and a quantitative water vapor budget analysis is not warranted in this configuration.

Acknowledgments

This research is funded by the National Natural Science Foundation of China No. 41930970 and No. 41776013. This research is partially supported by the International Laboratory for High-Resolution Earth System Prediction (iHESP). Dataset (ERA-INTERIM reanalysis) used in this work is publicly available to registered users at `https://www.ecmwf.int/en/forecasts/datasets/reanalysis-datasets/era-interim`

5 Appendix

5.1 Constructing the resample matrix for straightening interpolation

Perpendicular profiles are sampled along the AR axis to form the "resample matrix". Each perpendicular profile consists of one point on the AR axis (black dots in Fig. 1b), plus 14 evenly spaced points on the warm side of the AR covering a distance of 10° (∼ 1112 km, shown as red dots in Fig. 1b), and 21 evenly spaced points on the cold side, covering a distance of 15° (∼ 1668 km, blue dots in Fig. 1b). This gives a profile of $N = 35$ sample points with an even spacing of 0.71°, roughly the same as the native 0.75° resolution of the input ERA-I data. The asymmetry between the warm and cold sides is because an AR typically appears around an extratropical cyclone and a longer limb on the cold side helps capture the low pressure center of the cyclone.

Putting these oriented profiles into a regular array gives the resample matrix R, with a dimension of $N \times M$, where $N = 35$ is the number of points along each profile, and M the number of profiles. Unlike N that has a fixed value, the value of M varies as the AR length, therefore, it is further normalized (using bi-linear interpolation) to a fixed length of $M = 100$, making the straightened image composite-ready. The target grid to interpolate onto has the same shape as R but with x-coordinates being the AR length and the y-coordinates the AR width, both measured in km.

The direction of the profile is determined by finding a unit vector ($\boldsymbol{\theta_i}$) at each interior axis point (P_i) that evenly divide the angle formed by two consecutive line segments ($\overline{P_i, P_{i-1}}$ and $\overline{P_i, P_{i+1}}$). Formally, let $P_i = (x_i, y_i, z_i)$ and $P_{i+1} = (x_{i+1}, y_{i+1}, z_{i+1})$ being two consecutive points on the AR axis, and O being the origin of the unit sphere on which the Cartesian coordinates x, y, z are defined. Then the vector $\boldsymbol{T_{i,i+1}}$ tangent at P_i in the plane formed by $\overline{OP_i}$ and $\overline{OP_{i+1}}$ can be found by:

$$\boldsymbol{T_{i,i+1}} = (\boldsymbol{P_i} \times \boldsymbol{P_{i+1}}) \times \boldsymbol{P_i} = \boldsymbol{P_{i+1}} - \boldsymbol{P_i}(\boldsymbol{P_i} \cdot \boldsymbol{P_{i+1}}) \tag{1}$$

where $\times$ is cross product. Another tangent $\boldsymbol{T_{i,i-1}}$ can be similarly found. Using this definition, $\boldsymbol{\theta_i}$ can be defined as the average of the two unit tangents at P_i

$$\boldsymbol{\theta_i} = \frac{1}{2}\left(\frac{\boldsymbol{T_{i,i+1}}}{\|\boldsymbol{T_{i,i+1}}\|} + \frac{\boldsymbol{T_{i,i-1}}}{\|\boldsymbol{T_{i,i-1}}\|}\right) \tag{2}$$

An exception to this that is when the two consecutive segments form a straight line, $\boldsymbol{\theta_i}$ will be a zero vector. In such cases $\boldsymbol{\theta_i}$ is chosen to be $\boldsymbol{\theta_{warm}}$ defined next.

The direction of the warm side is determined by the vector of the axis segment $\overline{P_i, P_{i+1}}$ rotated *clockwise* by 90 degrees:

$$\boldsymbol{\theta_{warm}} = -\hat{\mathbf{k}} \times \overline{P_i, P_{i+1}} \tag{3}$$

where $\hat{\mathbf{k}}$ is the unit vector of the vertical dimension. Recall that the AR axis is directed by definition, so will be the $\overline{P_i, P_{i+1}}$ vector. Then the sign of $\boldsymbol{\theta_i}$ is reversed (if needed) so that it always aligns with $\boldsymbol{\theta_{warm}}$ (in that their dot product being positive) and points towards the warm side. Note that this is effectively the opposite process to the thermal wind derivation where the direction of the horizontal temperature gradient is rotated *anti-clockwise* by 90 degrees to give the thermal wind direction. The cold side is simply the opposite to the warm side: $\boldsymbol{\theta_{cold}} \equiv -\boldsymbol{\theta_{warm}}$.

The angle of the profile line with respect to the North is defined as $\arccos(-\boldsymbol{\theta_{cold}} \cdot \boldsymbol{T_{i,N}})$, where $\boldsymbol{T_{i,N}}$ is the local tangent vector pointing towards the North.

5.2 Determining the average curvature of an AR's axis

The average axis curvature is defined as the angles formed by consecutive line segment pairs ($\alpha_i = \arccos(\overline{\mathbf{P_i}, \mathbf{P_{i-1}}} \cdot \overline{\mathbf{P_i}, \mathbf{P_{i+1}}}$) along the AR axis, summed over the axis ($\sum_i \alpha_i$). The cyclonic direction is defined as positive curvature and vice versa.

References

Alpert, P., Shay-El, Y., & Heifetz, E. (1995). A comment on the geostrophic wind divergence. *Quarterly Journal of the Royal Meteorological Society*, *121*, 227-228. doi: 10.1002/qj.49712152111

Arora, T., Dhir, R., & Mahajan, M. (2017). An algorithm to straighten the bent human chromosomes. In *2017 fourth international conference on image information processing (iciip)* (p. 1-6). doi: 10.1109/ICIIP.2017.8313772

Bao, J.-W., Michelson, S. A., Neiman, P. J., Ralph, F. M., & Wilczak, J. M. (2006). Interpretation of enhanced integrated water vapor bands associated with extratropical cyclones: Their formation and connection to tropical moisture. *Monthly Weather Review*, *134*, 1063-1080. doi: 10.1175/mwr3123.1

Benedetto, F. (1957). Analysis of the vortivity and divergence of the thermal wind in pure geostrophic flow. *Archiv für Meteorologie, Geophysik und Bioklimatologie Serie A*, *10*, 20-28. doi: 10.1007/bf02247826

Browning, K. (1985). Conceptual models of precipitation systems. *Meteor. Mag.*, *114*, 293-319.

Browning, K. A., & Monk, G. A. (1982). A simple model for the synoptic analysis of cold fronts. *Quarterly Journal of the Royal Meteorological Society*, *108*, 435–452. doi: https://doi.org/10.1002/qj.49710845609

Browning, K. A., & Pardoe, C. W. (1973). Structure of low-level jet streams ahead of mid-latitude cold fronts. *Quarterly Journal of the Royal Meteorological Society*, *99*, 619–638. doi: https://doi.org/10.1002/qj.49709942204

Browning, K. A., & Roberts, N. M. (1996). Variation of frontal and precipitation structure along a cold front. *Quarterly Journal of the Royal Meteorological Society*, *122*, 1845-1872. doi: 10.1002/qj.49712253606

Cordeira, J. M., Ralph, F. M., & Moore, B. J. (2013). The development and evolution of two atmospheric rivers in proximity to western north pacific tropical cyclones in october 2010. *Monthly Weather Review*, *141*, 4234-4255. doi: 10.1175/mwr-d-13-00019.1

Dacre, H. F., Clark, P. A., Martinez-Alvarado, O., Stringer, M. A., & Lavers, D. A. (2015). How do atmospheric rivers form? *Bulletin of the American Meteorological Society*, *96*, 1243-1255. doi: 10.1175/BAMS-D-14-00031.1

Dacre, H. F., Martínez-Alvarado, O., & Mbengue, C. O. (2019). Linking atmospheric rivers and warm conveyor belt airflows. *Journal of Hydrometeorology*, *20*, 1183-1196. doi: 10.1175/jhm-d-18-0175.1

Dee, D. P., Uppala, S. M., Simmons, A. J., Berrisford, P., Poli, P., Kobayashi, S., ... Vitart, F. (2011). The era-interim reanalysis: configuration and performance of the data assimilation system. *Quarterly Journal of the Royal Meteorological Society*, *137*, 553–597. doi: 10.1002/qj.828

Eiras-Barca, J., Ramos, A. M., Pinto, J. G., Trigo, R. M., Liberato, M. L. R., & Miguez-Macho, G. (2018). The concurrence of atmospheric rivers and explosive cyclogenesis in the north atlantic and north pacific basins. *Earth System Dynamics*, *9*, 91-102. Retrieved from `http://dx.doi.org/10.5194/esd-9-91-2018` doi: 10.5194/esd-9-91-2018

Frenger, I., Gruber, N., Knutti, R., & Münnich, M. (2013). Imprint of southern ocean eddies on winds, clouds and rainfall. *Nature Geoscience*, *6*, 608-612. doi: 10.1038/ngeo1863

Gimeno, L., Nieto, R., VÃ¡zquez, M., & Lavers, D. A. (2014). Atmospheric rivers: a

mini-review. *Frontiers in Earth Science*, *2*. doi: 10.3389/feart.2014.00002

Held, I. M., & Soden, B. J. (2006). Robust responses of the hydrological cycle to global warming. *Journal of Climate*, *19*, 5686-5699. doi: 10.1175/JCLI3990.1

Holton, J. R., & Hakim, G. J. (2013). Chapter 9 - mesoscale circulations. In J. R. Holton & G. J. Hakim (Eds.), *An introduction to dynamic meteorology (fifth edition)* (Fifth Edition ed., p. 279 - 323). Boston: Academic Press. doi: https://doi.org/10.1016/B978-0-12-384866-6.00009-X

Hoskins, B. J., & Bretherton, F. P. (1972). Atmospheric frontogenesis models: Mathematical formulation and solution. *Journal of the Atmospheric Sciences*, *29*, 11-37. doi: 10.1175/1520-0469(1972)029⟨0011:afmmfa⟩2.0.co;2

Hoskins, B. J., & Hodges, K. I. (2002). New perspectives on the northern hemisphere winter storm tracks. *Journal of the Atmospheric Sciences*, *59*, 1041-1061. doi: 10.1175/1520-0469(2002)059⟨1041:NPOTNH⟩2.0.CO;2

Jahani, S., & Kamaledin Setarehdan, S. (2012). Centromere and length detection in artificially straightened highly curved human chromosomes. *International Journal of Biological Engineering*, *2*, 56-61. doi: 10.5923/j.ijbe.20120205.04

Jourdain, N. C., Barnier, B., Ferry, N., Vialard, J., Menkes, C. E., Lengaigne, M., & Parent, L. (2014). Tropical cyclones in two atmospheric (re)analyses and their response in two oceanic reanalyses. *Ocean Modelling*, *73*, 108-122. doi: 10.1016/j.ocemod.2013.10.007

Keyser, D., Reeder, M. J., & Reed, R. J. (1988). A generalization of petterssen's frontogenesis function and its relation to the forcing of vertical motion. *Monthly Weather Review*, *116*, 762-781. doi: 10.1175/1520-0493(1988)116⟨0762:agopff⟩2.0.co;2

Knaff, J. A., Longmore, S. P., & Molenar, D. A. (2014). An objective satellite-based tropical cyclone size climatology. *Journal of Climate*, *27*, 455-476. doi: 10.1175/JCLI-D-13-00096.1

Knippertz, P., Wernli, H., & Gläser, G. (2013). A global climatology of tropical moisture exports. *Journal of Climate*, *26*, 3031-3045. doi: 10.1175/jcli-d-12-00401.1

Liu, X., Ma, X., Chang, P., Jia, Y., Fu, D., Xu, G., ... Patricola, C. M. (2021). Ocean fronts and eddies force atmospheric rivers and heavy precipitation in western north america. *Nature Communications*, *12*. Retrieved from `http://dx.doi.org/10.1038/s41467-021-21504-w` doi: 10.1038/s41467-021-21504-w

Mundhenk, B. D., Barnes, E. A., & Maloney, E. D. (2016). All-season climatology and variability of atmospheric river frequencies over the north pacific. *Journal of Climate*, *29*(13), 4885-4903. doi: 10.1175/JCLI-D-15-0655.1

Neiman, P. J., Ralph, F. M., Moore, B. J., Hughes, M., Mahoney, K. M., Cordeira, J. M., & Dettinger, M. D. (2013). The landfall and inland penetration of a flood-producing atmospheric river in arizona. part i: Observed synoptic-scale, orographic, and hydrometeorological characteristics. *Journal of Hydrometeorology*, *14*, 460-484. doi: 10.1175/jhm-d-12-0101.1

Newell, R. E., & Zhu, Y. (1994). Tropospheric rivers: A one-year record and a possible application to ice core data. *Geophysical Research Letters*, *21*, 113-116. doi: 10.1029/93gl03113

Petterssen, S. (1936). Contribution to the theory of frontogenesis. *Geofys. Publ.*, *11*, 1-27.

Ralph, F. M., Dettinger, M. D., Cairns, M. M., Galarneau, T. J., & Eylander, J. (2018). Defining "atmospheric river": How the glossary of meteorology helped resolve a debate. *Bulletin of the American Meteorological Society*, *99*, 837-839. doi: 10.1175/bams-d-17-0157.1

Ralph, F. M., Dettinger, M. D., Rutz, J., Jonathan, & Waliser, D. E. (2020). *Atmospheric rivers*. Gewerbestrasse 11, 6330 Cham, Switzerland: Springer International Publishing. doi: 10.1007/978-3-030-28906-5

Ralph, F. M., Iacobellis, S. F., Neiman, P. J., Cordeira, J. M., Spackman, J. R., Waliser, D. E., ... Fairall, C. (2017). Dropsonde observations of total integrated water vapor transport within north pacific atmospheric rivers. *Journal of Hydrometeorology*, *18*, 2577-2596. doi: 10.1175/JHM-D-17-0036.1

Ralph, F. M., Neiman, P. J., & Rotunno, R. (2005). Dropsonde observations in low-level jets over the northeastern pacific ocean from caljet-1998 and pacjet-2001: Mean vertical-profile and atmospheric-river characteristics. *Monthly Weather Review*, *133*, 889-910. doi: 10.1175/mwr2896.1

Ralph, F. M., Neiman, P. J., & Wick, G. A. (2004). Satellite and caljet aircraft observations of atmospheric rivers over the eastern north pacific ocean during the winter of 1997/98. *Monthly Weather Review*, *132*, 1721–1745. doi: 10.1175/1520-0493(2004)132⟨1721:SACAOO⟩2.0.CO;2

Schultz, D. M., Keyser, D., & Bosart, L. F. (1998). The effect of large-scale flow on low-level frontal structure and evolution in midlatitude cyclones. *Monthly Weather Review*, *126*, 1767-1791. doi: 10.1175/1520-0493(1998)126⟨1767:teolsf⟩2.0.co;2

Sodemann, H., & Stohl, A. (2013). Moisture origin and meridional transport in atmospheric rivers and their association with multiple cyclones*. *Monthly Weather Review*, *141*, 2850-2868. doi: 10.1175/mwr-d-12-00256.1

Sohn, B. J., & Park, S. C. (2010). Strengthened tropical circulations in past three decades inferred from water vapor transport. *Journal of Geophysical Research Atmospheres*, *115*, D15112. doi: 10.1029/2009JD013713

Wernli, B. H., & Davies, H. C. (1997). A lagrangian-based analysis of extratropical cyclones. i: The method and some applications. *Quarterly Journal of the Royal Meteorological Society*, *123*, 467-489. doi: 10.1002/qj.49712353811

Wick, G. A., Neiman, P. J., & Ralph, F. M. (2013). Description and validation of an automated objective technique for identification and characterization of the integrated water vapor signature of atmospheric rivers. *IEEE Transactions on Geoscience and Remote Sensing*, *51*(4), 2166-2176. doi: 10.1109/TGRS.2012.2211024

Xu, G., Ma, X., Chang, P., & Wang, L. (2020a). A comparison of northern hemisphere atmospheric rivers detected by a new image-processing based method and magnitude-thresholding based methods. *Atmosphere*, *11*, 628. doi: 10.3390/atmos11060628

Xu, G., Ma, X., Chang, P., & Wang, L. (2020b). Image-processing-based atmospheric river tracking method version 1 (ipart-1). *Geoscientific Model Development*, *13*, 4639-4662. doi: 10.5194/gmd-13-4639-2020

Zahn, M., & Allan, R. P. (2011). Changes in water vapor transports of the ascending branch of the tropical circulation. *Journal of Geophysical Research*, *116*, D18111. doi: 10.1029/2011JD016206

Zhang, X., Ma, X., & Wu, L. (2019). Effect of mesoscale oceanic eddies on extratropical cyclogenesis: A tracking approach. *Journal of Geophysical Research: Atmospheres*, *124*, 6411-6422. doi: 10.1029/2019jd030595

Zhang, Z., Ralph, F. M., & Zheng, M. (2019). The relationship between extratropical cyclone strength and atmospheric river intensity and position. *Geophysical Research Letters*, *46*, 1814-1823. doi: 10.1029/2018gl079071

Zhou, Y., Kim, H., & Guan, B. (2018). Life cycle of atmospheric rivers: Identification and climatological characteristics. *Journal of Geophysical Research: Atmospheres*, *123*. doi: 10.1029/2018jd029180

Zhu, Y., & Newell, R. E. (1994). Atmospheric rivers and bombs. *Geophysical Research Letters*, *21*, 1999-2002. Retrieved from `http://dx.doi.org/10.1029/94gl01710` doi: 10.1029/94gl01710

Zhu, Y., & Newell, R. E. (1998). A proposed algorithm for moisture fluxes from atmospheric rivers. *Monthly Weather Review*, *126*, 725–735. doi: 10.1175/1520-0493(1998)126⟨0725:APAFMF⟩2.0.CO;2